The Astrophysical Journal, 919:41 (12pp), 2021 September 20 https://doi.org/10.3847/1538-4357/ac106d

Gravitational Wave Backgrounds from Coalescing Black Hole Binaries at Cosmic Dawn: An Upper Bound

Kohei Inayoshi[1], Kazumi Kashiyama[2,3], Eli Visbal[4], and Zoltán Haiman[5]

[1] Kavli Institute for Astronomy and Astrophysics, Peking University, Beijing 100871, People's Republic of China; inayoshi@pku.edu.cn
[2] Research Center for the Early Universe, Graduate School of Science, University of Tokyo, Bunkyo-ku, Tokyo 113-0033, Japan
[3] Department of Physics, Graduate School of Science, University of Tokyo, Bunkyo-ku, Tokyo 113-0033, Japan
[4] Department of Physics and Astronomy and Ritter Astrophysical Research Center, University of Toledo, Toledo, OH 43606, USA
[5] Department of Astronomy, Columbia University, New York, NY 10027, USA

Received 2021 March 26; revised 2021 June 25; accepted 2021 June 29; published 2021 September 22

Abstract

The successive discoveries of binary merger events by Advanced LIGO-Virgo have been revealing the statistical properties of binary black hole (BBH) populations. A stochastic gravitational wave background (GWB) is a useful tool to probe the cosmological evolution of those compact mergers. In this paper, we study the upper bound on a GWB produced by BBH mergers, whose stellar progenitors dominate the reionization process at the cosmic dawn. Since early reionization by those progenitors yields a high optical depth of the universe inconsistent with the Planck measurements, the cumulative mass density is limited to $\rho_\star \lesssim 10^7\, M_\odot\, \mathrm{Mpc}^{-3}$. Even with this upper bound, the amplitude of a GWB owing to the high-z BBH mergers is expected to be as high as $\Omega_{\rm gw} \simeq 1.48^{+1.80}_{-1.27} \times 10^{-9}$ at $f \simeq 25$ Hz, while their merger rate at the present day is consistent or lower than the observed GW event rate. This level of GWB is detectable at the design sensitivity of Advanced LIGO-Virgo and would indicate a major contribution of the high-z BBH population to the local GW events. The spectral index is expected to be substantially flatter than the canonical value of $\simeq 2/3$ generically produced by lower-redshift and less-massive BBHs. Moreover, if their mass function is more top heavy than in the local universe, the GWB spectrum is even more skewed toward lower frequencies, which would allow us to extract information on the mass function of merging BBHs at high redshifts.

Unified Astronomy Thesaurus concepts: Gravitational wave astronomy (675)

1. Introduction

Since the detections of gravitational waves (GWs) associated with compact binary mergers have opened a new window to explore our universe, the number of GW sources has been increasing substantially (Abbott et al. 2016a, 2016b, 2016c). Recently, a new catalog of 47 compact binary mergers including 44 binary black holes (BBHs) detected in Advanced LIGO-Virgo observing run O3a has been reported (Abbott et al. 2021a). With the updated sample, the estimation of the primary BH mass spectrum and BBH merger rate have been substantially improved.

The origin of such massive BBHs and their formation pathway have been extensively discussed based on the properties of detected BBHs (e.g., the distribution of mass and spin components). So far, various models have been proposed; through massive binary evolution in low-metallicity environments (Dominik et al. 2012; Kinugawa et al. 2014; Belczynski et al. 2016; Kinugawa et al. 2016; Inayoshi et al. 2017; van den Heuvel et al. 2017; Neijssel et al. 2019; Santoliquido et al. 2021), dynamical processes in dense stellar clusters and galactic nuclei (Portegies Zwart & McMillan 2000; Rodriguez et al. 2015; Mapelli 2016; O'Leary et al. 2016; Bartos et al. 2017; Stone et al. 2017; McKernan et al. 2018; Tagawa et al. 2020), and primordial BH formation (Nakamura et al. 1997; Sasaki et al. 2016; Ali-Haïmoud et al. 2017).

Referring to the redshift-dependent BBH merger rate, a larger number of BBHs would merge at earlier epochs and thus most of the individually unresolved mergers produce a GW background (GWB; Kowalska-Leszczynska et al. 2015; Dvorkin et al. 2016; Hartwig et al. 2016; Abbott et al. 2016a; Inayoshi et al. 2016b; Callister et al. 2020; Périgois et al. 2021; Abbott et al. 2021b). The detection of a GWB will be used to probe the formation epoch and efficiency of coalescing BBHs, constrain the mass function for massive star/BH populations initiated in the early universe, and even provide information on the history of cosmic reionization. More specifically, the existence of high-z, massive BBH populations (e.g., the remnant BHs of Population III stars; hereafter Population III stars) expected to typically form at $z \sim 10$–30 would produce a GWB detectable by LIGO-Virgo with a unique spectral shape that flattens significantly at ∼30 Hz, which is distinguishable from the spectral index of ∼2/3 generically produced by lower-redshift and less-massive BBHs (Inayoshi et al. 2016b). A recent population synthesis study also claimed a deviation of the spectral index from the canonical value if the Population III contribution is included (Périgois et al. 2021).

Massive stellar progenitors of merging BBHs formed at the cosmic dawn ($z \gtrsim 6$) are also efficient producers of ionizing radiation in the early universe and are expected to dominate the reionization process. Recently, Planck reported an updated estimate of the optical depth of the universe to electron scattering inferred from the cosmic microwave background (CMB) anisotropies; $\tau_{\rm e} \simeq 0.052 \pm 0.008$ (Planck Collaboration et al. 2020). This low value would give a stringent constraint on the star formation history and the total stellar mass budget available for BBH formation at higher redshifts (Visbal et al. 2015; Inayoshi et al. 2016b). Therefore, this constrains the amplitude of a GWB owing to BBH mergers originating from high-z populations.

In this paper, we study the upper bound of the GWB produced by BBH mergers taking into account the constraint on the cumulative stellar mass from cosmic reionization. We find that even with the upper bound, the GWB signal is still detectable at the Advanced LIGO-Virgo design sensitivity, while the merger rate at $z \simeq 0$ is consistent or lower than the observed GW event rate. Using the updated BBH properties from the LIGO-Virgo O3a observing run and the new value of τ_e, we infer a GWB spectral shape with a characteristic flattening, which is even more skewed toward lower frequencies if the mass function is more top heavy than in the local universe. This is also an updated study on our previous paper (Inayoshi et al. 2016b) published after the detection of the first source GW150914, in which a single value of the BH mass was assumed and the higher optical depth ($\tau_e \simeq 0.06 \pm 0.016$) provided by the previous Planck estimate (Ade et al. 2016).

The rest of this paper is organized as follows: in Section 2, we describe our reionization model and provide an upper bound on the stellar mass density at the cosmic dawn, consistent with the recent Planck result. In Section 3, we calculate the redshift-dependent merger rate of BBHs under the constraint from the reionization history. In Section 4, we present the expected GWB spectra for various BH mass distributions, and discuss the detectability of those GWB signals and possible implications. Finally, in Section 5, we summarize the conclusion of this paper. Throughout this paper, we assume a Λ cold dark matter (DM) cosmology consistent with the latest constraints from Planck (Planck Collaboration et al. 2020); $h = 0.6732$, $\Omega_m = 0.3158$, $\Omega_b = 0.02238$, and $Y_{He} = 0.247$.

2. The Upper Bound of the Stellar Mass Density in the Cosmic Dawn

In this paper, we consider two BBH populations originating from different cosmic star formation histories, which are referred to as low-z and high-z BBH populations, respectively. The low-z BBH population follows the *observed* cosmic star formation rate density (SFRD), which is characterized by $\dot{\rho}_\star \propto (1+z)^{2.7}$ at $z \lesssim 2$, has a peak at the cosmic noon around $z \simeq 2$, and declines $\dot{\rho}_\star \propto (1+z)^{-2.9}$ toward higher redshifts (Madau & Dickinson 2014). This SFRD is often used for estimating the merger rates of compact binaries in many previous studies in the literature (e.g., Abbott et al. 2016a, 2021b).

The observed SFRD of the low-z stellar population is not sufficient to reionize the universe by $z \sim 6$ and to then keep it ionized (e.g., Robertson et al. 2015),[6] unless a large fraction ($\gtrsim 20\%$) of ionizing photons can escape from galaxies to the intergalactic media (IGM; Madau & Dickinson 2014) or the production efficiency of ionizing photons is sufficiently high (e.g., massive stars with stripped envelopes via binary interactions; see Ma et al. 2016). Therefore, a stellar population formed in fainter, undetected galaxies must exist beyond $z > 6$; the star formation rate extends to higher redshifts and is responsible for the completion of cosmic reionization by $z = z_{\rm reion}$. In this paper, the high-z BBH population refers to BBHs originating from such high-z stellar components. Their star formation activity is expected to take place in metal-poor/low-metallicity environments, e.g., protogalaxies in DM halos with virial temperatures of $T_{\rm vir} \simeq 10^3$–10^4 K (Bromm & Yoshida 2011; Wise et al. 2012). Although the cosmic SFRD at $z \gtrsim z_{\rm reion}$ has not been constrained tightly by direct observations of star-forming high-z galaxies, the measurements of the optical depth of the universe to electron scattering imprinted into the CMB anisotropies would give a constraint on the total stellar mass budget available for BBH formation at higher redshifts (Visbal et al. 2015; Inayoshi et al. 2016b). In this section, we give the upper bound of the total (comoving) mass density of stars at $z \gtrsim z_{\rm reion}$, depending on the physical parameters related to reionization processes.

2.1. The Semi-analytical Cosmic Reionization Model

We describe the redshift-dependent cosmic SFRD at $z \geqslant z_{\rm reion}$ using a phenomenological model with three fitting parameters:

$$\dot{\rho}_\star(z) = \frac{a_p}{1 + [(1+z)/b_p]^{c_p}} \quad \text{at } z \geqslant z_{\rm reion}. \tag{1}$$

This parameterization is motivated by the functional form used in Madau & Dickinson (2014), except the decline toward lower redshifts. If ionizing photons from star-forming galaxies lead the reionization process, the photon production rate per comoving volume is proportional to $\dot{\rho}_\star(z)$ as

$$\dot{n}_{\rm ion} = \frac{f_{\rm esc}\,\eta_{\rm ion}\,\dot{\rho}_\star(z)}{m_{\rm p}}, \tag{2}$$

where $f_{\rm esc}$ is the escape fraction of ionizing photons from galaxies to the IGM, $\eta_{\rm ion}$ is the ionizing photon number per stellar baryon, and $m_{\rm p}$ is the proton mass. Evidently, the two quantities have different values for each population depending on the typical properties of their host DM halos, initial mass function (IMF), and metallicity (see Yung et al. 2020a, 2020b, and references therein). Following previous studies (e.g., Greif & Bromm 2006; Johnson et al. 2013; Visbal et al. 2020; Liu & Bromm 2020a), we adopt fiducial values of $f_{\rm esc} = 0.1$ and $\eta_{\rm ion} = 4 \times 10^3$ for stellar populations that form in early protogalaxies and dominate the reionization process (e.g., Wise et al. 2014; $f_{\rm esc} \simeq 0.1$ for DM halos with $\gtrsim 10^8\,M_\odot$). Note that the value of $\eta_{\rm ion}$ is consistent with that of a $Z \simeq 0.02\,Z_\odot$ stellar population (hereafter, Population II)[7], which follows a Salpeter IMF with a mass range of 0.1–100 $M_\odot$. Since these values are uncertain, we also discuss the dependence on the product $f_{\rm esc}\eta_{\rm ion}$ that matters rather than their individual values.[8]

With the photon production rate, the IGM ionized volume fraction $Q_{\rm H_{II}}(z)$ is calculated by the differential equation (e.g., Haiman & Loeb 1997; Madau et al. 1999; Wyithe & Loeb 2003; Haiman & Bryan 2006),

$$\frac{dQ_{\rm H_{II}}}{dt} = \frac{\dot{n}_{\rm ion}}{\langle n_{\rm H}\rangle} - \frac{Q_{\rm H_{II}}}{t_{\rm rec}}, \tag{3}$$

---

[6] Robertson et al. (2015) computed the SFRD by extrapolating the actual observed luminosity function to a faint, unobserved value of $L_{\rm min} = 0.001\,L_\star$, where $L_\star$ is the characteristic luminosity of each parameterization, e.g., Schechter or broken power-law models (see also discussion by Madau & Dickinson 2014).

[7] Relatively metal-enriched stellar populations with smaller $\eta_{\rm ion}$ could contribute to the reionization process at $z > 6$ if the metallicity of galaxies decline toward high redshifts as weakly as seen at $z \simeq 2$–3 (Sanders et al. 2021; Suzuki et al. 2021).

[8] Recent submillimeter observations have revealed the existence of star-forming massive galaxies at $z > 2$ that are highly obscured by dust grains (e.g., Wang et al. 2019; Gruppioni et al. 2020). This galaxy population might not significantly contribute to the reionization process (presumably smaller values of $f_{\rm esc}$), but they still would produce a large amount of stars that potentially constitute another source of BBHs (Boco et al. 2019, 2021). Throughout this paper, however, their contribution to the BBH merger rate is not explicitly considered.

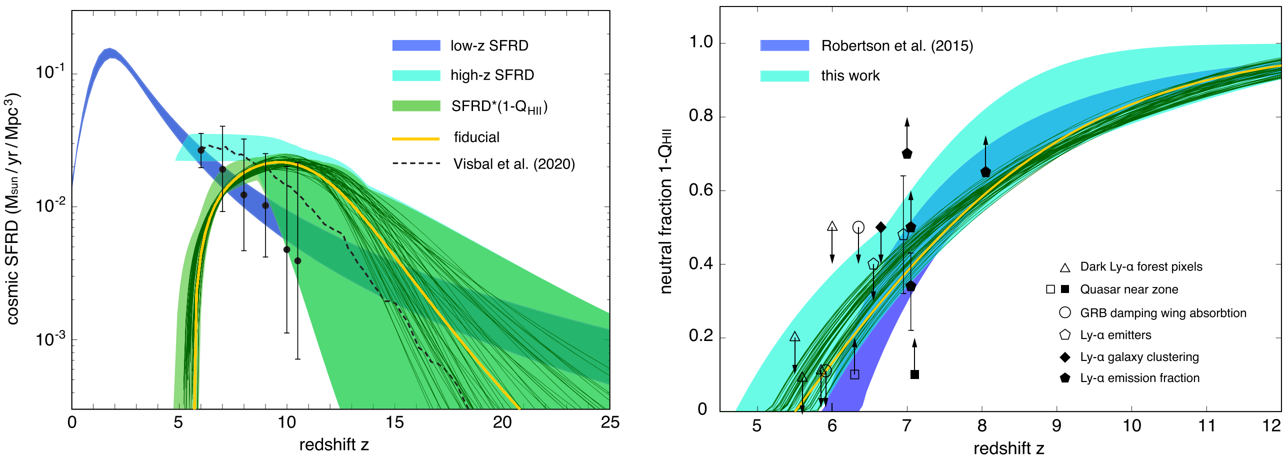

Figure 1. Left panel: cosmic SFRDs of the stellar population at $z \gtrsim 5$ (light-blue region), for which the Planck result ($\tau_{\rm e} = 0.0522 \pm 0.0080$ and $z_{\rm reion}^{50\%} = 7.50 \pm 0.82$) are consistently reproduced. The green region presents the SFRD in neutral regions before the completion of reionization, and the solid curves show 50 cases that form stars with $\rho_\star \simeq 10^7\, M_\odot\, {\rm Mpc}^{-3}$. Our fiducial SFRD model is highlighted with the yellow curve. For references, we overlay other SFRDs for the high-z population (black dashed line; Visbal et al. 2020) and for the low-z population (blue region; Madau & Dickinson 2014; Robertson et al. 2015) together with the errors of the observed SFRD at $z \gtrsim 6$ (Robertson et al. 2015). Right panel: evolution of cosmic volume fraction of neutral regions $1 - Q_{\rm H_{II}}(z)$ in our model (light-blue region, green curves, and yellow curve), together with the observational constraints compiled by Robertson et al. (2015) and the result consistent with the previous Planck estimate (blue region).

where the IGM recombination time is given by

$$t_{\rm rec} = \left[C_{\rm H_{II}} \alpha_{\rm B} \left(1 + \frac{Y_{\rm He}}{4X_{\rm H}}\right) \langle n_{\rm H} \rangle (1+z)^3 \right]^{-1}, \tag{4}$$

$\alpha_{\rm B}$ is the case B recombination coefficient at an IGM temperature of $T = 2 \times 10^4$ K, $\langle n_{\rm H} \rangle$ is the IGM mean comoving number density of hydrogen, $C_{\rm H_{II}} \equiv \langle n_{\rm H_{II}}^2 \rangle / \langle n_{\rm H_{II}} \rangle^2$ is a clumping factor of ionized hydrogen, and $X_{\rm H} = 0.76$ and $Y_{\rm He} = 0.24$ are the hydrogen and helium mass fractions. We adopt $C_{\rm H_{II}} = 4$ (e.g., Pawlik et al. 2009; Robertson et al. 2015). Finally, for a given reionization history associated with an SFRD model, the optical depth $\tau_{\rm e}$ is calculated with

$$\tau_{\rm e}(z) = c \langle n_{\rm H} \rangle \sigma_{\rm T} \int_0^z Q_{\rm H_{II}}(z') \frac{(1+z')^2}{H(z')} \left(1 + \frac{\eta_{\rm He} Y_{\rm He}}{4X_{\rm H}}\right) dz', \tag{5}$$

where c is the speed of light, $\sigma_{\rm T}$ is the cross section of Thomson scattering, and $H(z)$ is the Hubble parameter. Helium is assumed to be singly ionized with hydrogen at $z \geqslant 3$ ($\eta_{\rm He} = 1$), but be doubly ionized at the lower redshifts ($\eta_{\rm He} = 2$).

In this framework, we investigate the ranges of the three parameters (a_p, b_p, and c_p) in Equation (1), which are constrained from (i) the SFRD estimated from UV luminosities at $z \simeq 6$ (Robertson et al. 2015), (ii) the Planck measured optical depth $\tau_{\rm e} = 0.0522 \pm 0.0080$, and (iii) reionization redshift midpoint $z_{\rm reion}^{50\%} = 7.50 \pm 0.82$ (Planck Collaboration et al. 2020). We note that those values of $\tau_{\rm e}$ and $z_{\rm reion}^{50\%}$ are estimated for a specific shape of $Q_{\rm H_{II}}(z)$ and the resultant shape obtained from our semi-analytical model is similar to those assumed by the Planck team. A recent paper by Ahn & Shapiro (2021) showed with a suite of models of early reionization due to Population III stars (see also our discussion in Section 2.3), their best-fit models to the Planck polarization data go up to $\tau_{\rm e} \simeq 0.064$. Therefore, the optical depth we adopt is a conservative choice.

2.2. The Upper Bound of the Total Stellar Mass

First, we consider the case where a single stellar population dominates the reionization process, that is, a single value of $f_{\rm esc}\eta_{\rm ion}$(=400) is adopted at all redshifts. In the left panel of Figure 1, we show the range of cosmic SFRDs at $z \gtrsim 5$, for which the Planck measured values of $\tau_{\rm e}$ and $z_{\rm reion}^{50\%}$ are consistently reproduced (light-blue region). Those SFRDs are as high as $\dot{\rho}_\star \sim (2–4) \times 10^{-2}\, M_\odot\, {\rm yr}^{-1}\, {\rm Mpc}^{-3}$ at $z \lesssim 9$ and begin to decline toward high redshifts at $z \gtrsim 10–14$. All the cases shown here are consistent with the observed SFRDs within the errors over $5 \lesssim z \lesssim 10.5$ and smoothly connect to the SFRD measured at lower redshifts (blue region; Madau & Dickinson 2014 and Robertson et al. 2015). For comparison, we overlay an SFRD model calculated by Visbal et al. (2020), where more realistic prescriptions for star formation, radiation feedback, IGM metal pollution, and the transition from Population III to Population II stars are considered. In the right panel of Figure 1, we present the neutral fraction ($1 - Q_{\rm H_{II}}$) of the IGM as a function of redshift, together with the observational constraints compiled by Robertson et al. (2015, and references therein). The computed reionization history is overall consistent with these observational results. The result consistent with the previous Planck estimate (blue region) is overlaid for comparison.

In this paper, we consider a GWB produced by stellar populations that contribute to cosmic reionization and presumably form in DM halos with $T_{\rm vir} \lesssim 2 \times 10^4$ K, where gas is vulnerable to photoionization heating feedback (e.g., Dijkstra et al. 2004; Okamoto et al. 2008). Therefore, we assume that the formation of the early component is suppressed in ionized regions and thus takes place only in neutral regions with a cosmic volume fraction of $1 - Q_{\rm H_{II}}(z)$.[9] The SFRDs of such populations are shown with the green shaded region, which

---

[9] There would exist metal-free DM halos that are massive enough to overcome the photoionization heating feedback and make Population III stars even in ionized regions of the IGM after reionization (Johnson 2010; Kulkarni et al. 2019). Although such a formation pathway of Population III stars is allowed without violating the Planck constraint, we here do not consider their remnant (binary) BHs as the high-z population.

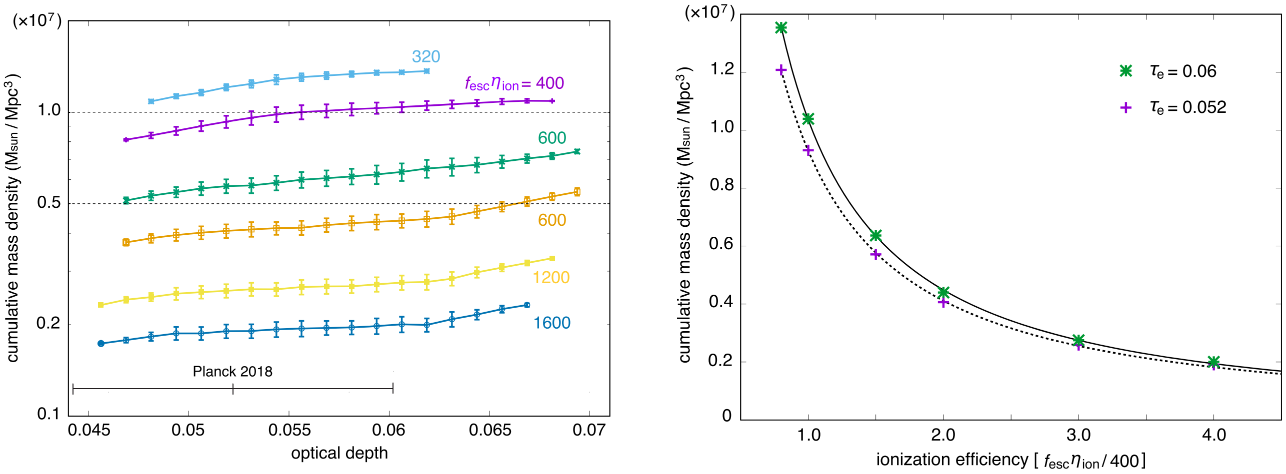

Figure 2. Left panel: cumulative stellar mass density consistent with the Planck measurements as a function of the ionization efficiency; $f_{\rm esc}\eta_{\rm ion} = 320$, 400 (fiducial), 600, 800, 1200, and 1600 from the top to the bottom (the 1σ errors are shown in each $\tau_{\rm e}$ bin with a size of 1.25×10^{-3}). The range of $\tau_{\rm e}$ inferred from the Planck observation is shown (Planck Collaboration et al. 2020). Right panel: The relation between $\rho_\star$ and $f_{\rm esc}\eta_{\rm ion}$ is shown for the two cases of $\tau_{\rm e} = 0.052$ and 0.06. The results are well approximated by Equation (7).

peaks around $z \simeq z_{\rm reion}^{50\%}$ and sharply drops at $z \simeq z_{\rm reion}$. For each model, we calculate the cumulative stellar mass density defined by

$$\rho_\star = \int_{z_{\rm reion}}^{\infty} \dot{\rho}_\star(z)\{1 - Q_{\rm H_{II}}(z)\}\frac{dt}{dz}dz. \tag{6}$$

In the left panel of Figure 2, we present the cumulative stellar mass density as a function of $\tau_{\rm e}$ for the cases with different values of $\eta_{\rm ion} f_{\rm esc} = 320$, 400 (fiducial), 600, 800, 1200, and 1600 from the top to the bottom (the 1σ errors are shown in each $\tau_{\rm e}$ bin with a size of 1.25×10^{-3}). Note that $z_{\rm reion}^{50\%} = 7.50 \pm 0.82$ is satisfied for all the cases. For the fiducial case, the cumulative mass density is as high as $\rho_\star \simeq 10^7\, M_\odot\, {\rm Mpc}^{-3}$ and depends on the optical depth as $\propto \tau_{\rm e}^{0.68}$. Within the uncertainty of $\tau_{\rm e} = 0.0522 \pm 0.008$ (Planck Collaboration et al. 2020), the value of $\rho_\star$ varies within $\simeq$0.1 dex. With higher values of $f_{\rm esc}\ \eta_{\rm ion}$, the cumulative mass density decreases so that the resultant optical depth becomes consistent with that measured by the Planck. In the right panel of Figure 2, we show the dependence of $\rho_\star$ on $f_{\rm esc}\ \eta_{\rm ion}$ for the two cases of $\tau_{\rm e} = 0.052$ and 0.06. For both cases, the results are well fitted with a single power law of $\rho_\star/(10^7\, M_\odot\, {\rm Mpc}^{-3}) = a_q(f_{\rm esc}\eta_{\rm ion}/400)^{-b_q}$, where $a_q = 1.04$ (0.929) and $b_q = 1.21$ (1.18) for $\tau_{\rm e} = 0.06$ (0.052). Therefore, we obtain the relation between the total stellar mass density formed by the end of reionization and the physical parameters of the reionization process

$$\rho_\star \simeq 1.04 \times 10^7\, M_\odot\, {\rm Mpc}^{-3} \times \left(\frac{f_{\rm esc}}{0.1}\right)^{-1.2}\left(\frac{\eta_{\rm ion}}{4 \times 10^3}\right)^{-1.2}\left(\frac{\tau_{\rm e}}{0.06}\right)^{0.68}. \tag{7}$$

We note that the mass density is broadly consistent with cosmological hydrodynamical simulations for high-z galaxy formation (e.g., Johnson et al. 2013). The value in Equation (7) is considered to be the *upper bound* of the stellar mass formed at $z \gtrsim z_{\rm reion}$ since it would be lowered if other rarer but more intense radiation sources (e.g., metal-free Population III stars and high-z quasars) could contribute to reionization (Visbal et al. 2015; Dayal et al. 2020, see also Section 2.3).

Among all the SFRD models consistent with the Planck result, we show 50 cases with $\rho_\star = 1.0^{+0.1}_{-0.1} \times 10^7\, M_\odot\, {\rm Mpc}^{-3}$ (green thin curves in Figure 1), which are characterized with a functional form of

$$\dot{\rho}_{\star,{\rm reion}}(z) = \frac{a_p \cdot \tanh[(z - z_{\rm reion})/d_p]}{1 + [(1 + z)/b_p]^{c_p}} \tag{8}$$

at $z \geqslant z_{\rm reion}$, where we fit the evolution of $1 - Q_{\rm H_{II}}(z) = \tanh[(z - z_{\rm reion})/d_p]$, consistent with the Planck analysis. In this paper, we adopt one of them as our fiducial SFRD model with $a_p = 0.032\, M_\odot\, {\rm yr}^{-1}\, {\rm Mpc}^{-3}$, $b_p = 13$, $c_q = 9$, $d_p = 3.74$, and $z_{\rm reion} = 5.5$, yielding $\rho_\star = 1.0 \times 10^7\, M_\odot\, {\rm Mpc}^{-3}$ and $\tau_{\rm e} = 0.06$ (yellow curves in Figure 1).

2.3. The Upper Bound of the Population III Stellar Mass

Next, we consider the impact of metal-free Population III stars on the reionization history and give the upper bound of their total mass formed across cosmic time. Population III stars are predicted to be more efficient at producing ionizing radiation than metal-enriched Population II stars (Schaerer 2002, 2003). If Population III stars form with a top-heavy IMF, the ionization efficiency is substantially enhanced (e.g., $\eta_{\rm ion} = 5.1 \times 10^4$ for a Salpeter IMF with 10–100 $M_\odot$). Moreover, a fraction of Population III stars would form in less-massive DM halos with $\lesssim 10^7\, M_\odot$, where the escape fraction of ionizing photons is expected to be as high as $f_{\rm esc} \simeq 0.5$. Therefore, Population III stars would affect the reionization history and create an early partial reionization, which leads to a higher optical depth inconsistent with the Planck result (Visbal et al. 2015).

We repeat the same calculations but considering an effective ionization efficiency $\langle f_{\rm esc}\eta_{\rm ion}\rangle$ that includes the contribution of ionizing radiation from both Population II and Population III stars defined by

$$\langle f_{\rm esc}\eta_{\rm ion}\rangle\, \dot{\rho}_\star = f_{\rm esc}^{\rm II}\, \eta_{\rm ion}^{\rm II}\, \dot{\rho}_{\star,{\rm II}} + f_{\rm esc}^{\rm III}\, \eta_{\rm ion}^{\rm III}\, \dot{\rho}_{\star,{\rm III}}, \tag{9}$$

where $\dot{\rho}_{\star,{\rm III(II)}}$, $f_{\rm esc}^{\rm II(III)}$, and $\eta_{\rm ion}^{\rm II(III)}$ are the cosmic SFRD, escape fraction, and number of ionizing photons per stellar baryon for Population II(III) stars. When Population II stars dominate the total SFRD (i.e., $\dot{\rho}_\star \simeq \dot{\rho}_{\star,{\rm II}}$), the above equation is approximated

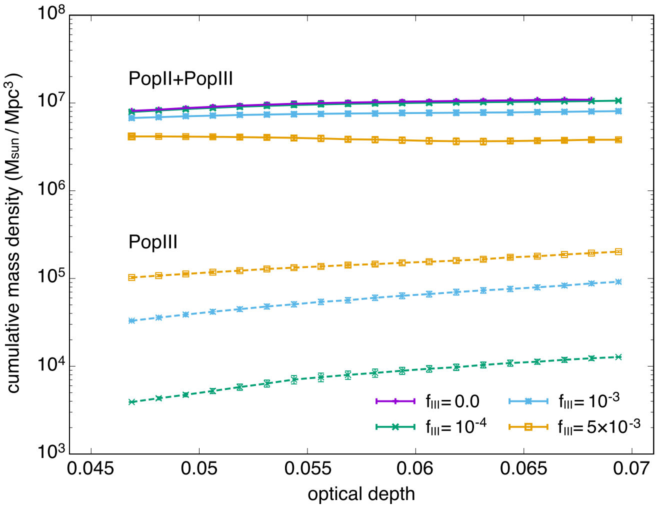

Figure 3. Cumulative stellar mass density of Population II+III (solid) and Population III (dashed) stars for different Population III star formation efficiencies of $f_{\rm III} = 10^{-4}$, 10^{-3}, and 5×10^{-3}. With a higher value of $f_{\rm III}$, the total amount of Population II stars gradually decreases because cosmic reionization is accelerated due to additional ionizing photons from Population III stars. In contrast, the Population III mass density increases up to $\lesssim 2 \times 10^5\, M_\odot\, {\rm Mpc}^{-3}$.

as

$$\langle f_{\rm esc}\eta_{\rm ion}\rangle \approx f_{\rm esc}^{\rm II}\eta_{\rm ion}^{\rm II}\left(1 + \mathcal{F}\frac{\dot\rho_{\star,\rm III}}{\dot\rho_{\star,\rm II}}\right), \tag{10}$$

where $\mathcal{F} \equiv f_{\rm esc}^{\rm III}\eta_{\rm ion}^{\rm III}/(f_{\rm esc}^{\rm II}\eta_{\rm ion}^{\rm II}) \sim O(10 - 100)$, and the ratio of $\dot\rho_{\star,\rm III}/\dot\rho_{\star,\rm II}$ tends to increase with redshift but the functional shape depends on the prescriptions for Population III star formation. As a reference, Visbal et al. (2020) shows that the ratio is well approximated by $\dot\rho_{\star,\rm III}/\dot\rho_{\star,\rm II} \approx 0.2\,(f_{\rm III}/10^{-3})[(1 + z)/31]^3$ at $z < 30$, where $f_{\rm III}$ is the Population III star formation efficiency from gas clouds. Note that the functional form of $\dot\rho_{\star,\rm III}/\dot\rho_{\star,\rm II}$ depends on the modeling of Population III star formation. We here adopt the fiducial model in Visbal et al. (2020); see also other Population III models described in Liu & Bromm (2020a), where the SFRD seems consistent with our model with $f_{\rm III} = 10^{-3}$ but tends to be higher at higher redshifts ($z > 6$), leading to a higher optical depth even with the similar amount of Population III stars.

In Figure 3, we present the cumulative stellar mass density of Population II+III (solid) and Population III (dashed) stars for three values of $f_{\rm III} = 10^{-4}$, 10^{-3}, and 5×10^{-3}. We here adopt $f_{\rm esc}^{\rm II} = 0.1$, $f_{\rm esc}^{\rm III} = 0.5$, $\eta_{\rm ion}^{\rm II} = 4 \times 10^3$, and $\eta_{\rm ion}^{\rm II} = 5.1 \times 10^4$. With a higher value of $f_{\rm III}$, the total amount of Population II stars decreases gradually so that the total photon budget is adjusted to be consistent with the reionization history. In contrast, the Population III mass density increases with $f_{\rm III}$ but does not linearly scale with $f_{\rm III}$ at $\gtrsim 10^{-3}$ because the total mass budget is regulated. Overall, the mass density of Population III stars is limited to $\lesssim 2 \times 10^5\, M_\odot\, {\rm Mpc}^{-3}$ and thus their contribution to the total stellar mass formed in the epoch of reionization is at most $\lesssim 2\%$. Note that the upper bound of the Population III mass density is broadly consistent with the value estimated in Visbal et al. (2015), where the optical depth quoted from the Planck 2015 result (Ade et al. 2016) was used.

3. Redshift-dependent BH Merger Rates

3.1. Properties of BBH Mergers Implied by LIGO-Virgo O3a Run

With the updated BBH sample in the GWTC-2 catalog (Abbott et al. 2021a), the mass spectrum for the primary BH in merging binaries, $d\mathcal{R}_{\rm BBH}/dM_1$, is found to be characterized by a broken power law with a break at $39.7^{+20.3}_{-9.1}\, M_\odot$, or a power law with a Gaussian feature peak at $33.5^{+4.5}_{-5.5}\, M_\odot$. The functional form of the broken power-law mass spectrum is given by

$$\frac{d\mathcal{R}_{\rm BBH}}{dM_1} \propto \begin{cases} M_1^{-\alpha_1} & \text{for } M_{\rm min} < M_1 \leqslant M_{\rm break},\\ M_1^{-\alpha_2} & \text{for } M_{\rm break} < M_1 < M_{\rm max},\\ 0 & \text{otherwise,}\end{cases} \tag{11}$$

where $\alpha_1 = 1.58$, $\alpha_2 = 5.59$, $M_{\rm min} = 3.96\, M_\odot$, and $M_{\rm max} = 87.14\, M_\odot$ are adopted, $M_{\rm break} = M_{\rm min} + bM_{\rm max}$ is the mass where there is a break in the spectral index ($b = 0.43$), and the smoothing function at $M_{\rm min} < M_1 < M_{\rm min} + \delta_M$ ($\delta_M = 4.83\, M_\odot$) is taken into account (Abbott et al. 2021a). With the mass spectrum, the average BH mass is calculated by

$$\langle M_1\rangle \equiv \frac{\int_{M_{\rm min}}^{M_{\rm max}} M_1 \frac{d\mathcal{R}_{\rm BBH}}{dM_1}\, dM_1}{\int_{M_{\rm min}}^{M_{\rm max}} \frac{d\mathcal{R}_{\rm BBH}}{dM_1}\, dM_1}. \tag{12}$$

For the broken power-law mass spectrum that does not evolve with redshift, the average mass of the primary BH is $\langle M_1\rangle = 17.5\, M_\odot$ and the average total mass in a binary is $\langle M_{\rm tot,b}\rangle \equiv (1 + q)\langle M_1\rangle = 35 M_\odot[(1 + q)/2]$, where q is the mass ratio of the two BHs. In this paper, we adopt this mass spectrum as our fiducial model (see Section 4.1).

The LIGO-Virgo observing O3a run has well constrained the mass-integrated merger rate defined by

$$R_{\rm BBH}(z) \equiv \int \frac{d\mathcal{R}_{\rm BBH}}{dM_1} dM_1. \tag{13}$$

The merger rate estimated from the GW events detected by the LIGO-Virgo O1+O2+O3 runs is found to increase with redshift as $R_{\rm BBH}(z) = R_{\rm BBH,0}(1 + z)^\kappa$, where $R_{\rm BBH,0} \simeq 19.1^{16.2}_{-9.0}\ {\rm Gpc}^{-3}\ {\rm yr}^{-1}$ and $\kappa = 1.8^{+9.6}_{-9.5}$ ($1.3^{+2.1}_{-2.1}$) for the broken power-law (power-law + peak) mass spectrum (Abbott et al. 2021a).

3.2. Modeling the BBH Merger Rate

The redshift-dependent BBH merger rate is given by a convolution of the delay-time distribution (DTD) $\Psi(t)$ for binary coalescences and the BBH formation rate $\dot\rho_{\rm BBH}(t)$;

$$R_{\rm BBH}(z) = \frac{1}{\langle M_{\rm tot,b}\rangle}\int_0^{t(z)} \dot\rho_{\rm BBH}(t')\Psi(t - t')dt', \tag{14}$$

where $t(z)$ is the cosmic time at redshift z and the average mass in a BBH is assumed to be constant. Here, we adopt a power-law distribution of the delay time,

$$\Psi(t) = \frac{\Psi_0}{t_{\rm min}}\left(\frac{t}{t_{\rm min}}\right)^{-n} \quad \text{for } t_{\rm min} < t < t_{\rm max}, \tag{15}$$

and $\Psi(t) = 0$ otherwise, where $t_{\rm min(max)}$ is the minimum (maximum) merger timescale for binaries. The normalization of

Ψ_0 is determined so that the integration of Equation (15) from $t_{\rm min}$ to $t_{\rm max}$ is unity. We consider the maximum merger time, which depends on the maximum binary separation, to be significantly longer than a Hubble time ($t_{\rm max} \gg t_{\rm H}$). Here, we adopt $t_{\rm max} = 10^3\, t_{\rm H}$. We note that the choice of $t_{\rm max}$ is not important for $n \gtrsim 1$, which we mainly focus on in the following discussion. This type of the DTD is inspired by those of the GW-driven inspirals ($n \simeq 1$; see Piran 1992) and other astrophysical phenomena related to binary mergers. For instance, the DTD of type Ia supernovae has $n \simeq 1$ and $t_{\rm min}$ of 40 Myr to a few hundreds of megayears (Maoz et al. 2014 and references therein), and that of short GRBs has $n \simeq 1$ and $t_{\rm min} \simeq 20$ Myr (Wanderman & Piran 2010; Ghirlanda et al. 2016). Population synthesis calculations reproduce DTDs with $n \simeq 1$ for BBH mergers that hardly depend on the binary properties and their formation redshifts (Dominik et al. 2012; Kinugawa et al. 2014; Tanikawa et al. 2021). Recently, Safarzadeh et al. (2020) discussed the effects of the delay-time nature of BBHs on the stochastic GWB amplitude.

For the cosmic BBH formation rate, we consider two scenarios: (i) BBH formation follows the observed cosmic SFRD (Madau & Dickinson 2014) for the low-z BBH population and (ii) BBH formation follows the SFRD given by Equation (8) for the high-z BBH population. The total stellar mass densities are $\rho_\star \simeq 5.7^{+1.7}_{-1.9} \times 10^8\, M_\odot\ {\rm Mpc}^{-3}$ for the low-z population (Madau & Dickinson 2014, and references therein) and $\rho_\star \lesssim 10^7\, M_\odot\,{\rm Mpc}^{-3}$ for the high-z population (see Equation (7)). The cosmic BBH formation rate is given by calculating a mass fraction $f_{\rm BBH}\,(\equiv \dot{\rho}_{\rm BBH}/\dot{\rho}_\star)$ of BBHs merging within $t_{\rm max}$ to the total stellar mass. The merging-BBH formation efficiency $f_{\rm BBH}$ is estimated as a product of the following three fractions:

1. The first one is the mass fraction of massive stars forming BHs in a given mass budget. Nonrotating stars of zero-age main-sequence mass $M \gtrsim M_\bullet = 20\, M_\odot$ are expected to leave remnant BHs via gravitational collapse at the end of their lifetime (e.g., Spera & Mapelli 2017). The mass fraction is estimated for a given IMF of $dN/dM\,(\propto M^{-\alpha})$ by
$$f_\bullet \equiv \frac{\int_{M_\bullet}^{M_{\star,\rm max}} M \frac{dN}{dM} dM}{\int_{M_{\star,\rm min}}^{M_{\star,\rm max}} M \frac{dN}{dM} dM}. \qquad (16)$$
For a Salpeter IMF ($\alpha = 2.35$) with a mass range of 0.1(1)–100 $M_\odot$, we estimate $f_\bullet \simeq 0.074\,(0.189)$.[10] However, as discussed in many previous studies in the literature, the stellar evolution for such massive stars would suffer from a significant mass loss unless they are low-metallicity stars with $Z \lesssim Z_{\rm crit} \sim 0.1\, Z_\odot$ (Abbott et al. 2016b, and references therein) and the value of $f_\bullet$ would be lower with the metallicity increasing. There are also several lines of observational evidence that the fraction of high-mass X-ray binaries increases with redshift and the trend would be explained by the lack of metallicity at higher redshifts (Crowther et al. 2010; Mirabel et al. 2011; Fragos et al. 2013; Mirabel 2019). Although we do not specify the metallicity range of the high-z stellar population, we implicitly assume $Z \sim 0.02\, Z_\odot$ consistent with the production rate of ionizing radiation we adopt in Section 2.1. We also note that even with $Z \lesssim 0.1\, Z_\odot$, the remnant mass of massive stars would be affected by pulsation-driven winds in the main-sequence and giant phases (Nakauchi et al. 2020) and by (pulsational) pair-instability supernovae in the later phases (Spera & Mapelli 2017; Woosley 2017), although the mass and metallicity criteria for the mass-loss process depend on the nuclear burning rate of $^{12}{\rm C}(\alpha, \gamma)^{16}{\rm O}$ and the treatments of stellar convection (e.g., Farmer et al. 2020; Costa et al. 2021).
2. Second, we assume that those massive stars that will collapse to BHs have a binary companion at a fraction of $f_{\rm bin} \simeq 0.7$, which is consistent with the field binary fraction of O-type stars at the present ($f_{\rm bin} \simeq 0.69 \pm 0.09$) (Sana et al. 2012). Local observations suggest that the mass-ratio q distribution is characterized by a power law of q^{β_q}, where $\beta_q = -0.1 \pm 0.58$ (Sana et al. 2012) and $\beta_q = 0.1 \pm 0.3$ (Moe & Di Stefano 2017) over $0.3 \lesssim q \lesssim 1$. However, there are no observational constraints on the q distribution for low-metallicity massive binaries that are considered to be the progenitors of BBHs. On the other hand, the power-law index for BBH mergers is inferred from LIGO-Virgo detections as $\beta_q = 1.4^{+2.5}_{-1.5}$, suggesting a concentration to $q \simeq 1$. In this paper, we assume the mass ratio to be unity $q = 1$ for simplicity, which provides an upper bound of $f_{\rm BBH}$ (i.e., a massive star has a massive binary companion at a chance of $f_{\rm bin}$).
3. Third, only a fraction $f_{\rm mrg}$ of the massive binaries end up as BBHs merging within $t_{\rm max}$ due to shorter initial binary separations and/or hardening process through binary interactions. Assuming that Öpik's law is applied to massive binaries, the cumulative distribution of primordial binary separations is logarithmically flat between $a_{\rm min} \simeq 10\, R_\odot$ and $a_{\rm max} \simeq 10^6\, R_\odot$.[11] Truncating the distribution at $a \simeq 1$ au, for which the GW merger timescale is $\simeq t_{\rm max}$, the fraction is estimated as $f_{\rm mrg} \simeq 0.26$. The orbital-period distribution of observed O-type stars would prefer close binaries more than predicted by Öpik's law (Sana et al. 2012; Moe & Di Stefano 2017), suggesting a larger value of $f_{\rm mrg}$. In such close binaries, however, their orbital evolution is likely affected by binary interactions (e.g., mass transfer, tidal effect, and common envelope phases) before they form BBHs and thus the processes bring large uncertainties for estimating $f_{\rm mrg}$. Moreover, with higher metallicities ($Z \gtrsim Z_{\rm crit}$), mass loss from a binary system makes the binary separation significantly wider and its merger timescale much longer than $t_{\rm max}$.

Using the three fractions, we calculate the merging-BBH formation efficiency as $f_{\rm BBH} = f_\bullet f_{\rm mrg} \left(\frac{2 f_{\rm bin}}{1 + f_{\rm bin}}\right)$. For the high-$z$ BBH scenario, we adopt $f_{\rm BBH} \simeq 0.018$ for our fiducial case ($f_\bullet = 0.074, f_{\rm bin} = 0.7$, and $f_{\rm mrg} = 0.3$), although a higher value of $f_\bullet$ would be expected for more top-heavy IMF of low-metallicity

---

[10] For the Salpeter IMF, the average mass of massive stars with $M \geqslant M_\bullet$ is estimated as $\langle M_\star \rangle \simeq 37\, M_\odot$, which is larger than the average mass of the primary BH. We note that if we use $\langle M_\star \rangle$ instead of $\langle M_1 \rangle = 17\, M_\odot$, the merger rate in Equation (14) is reduced by a factor of $\sim$2 and the GWB spectrum is skewed to lower frequencies, but the total GWB energy density is not affected (see also Section 4.2). This twofold difference in the merger rate can be absorbed in the uncertainty of $f_\bullet$ by changing $M_{\rm min}$ from 0.1–1 $M_\odot$.

[11] Note that the minimum separation is set so that the primary star does not fill its Roche lobe at the minimum separation, namely, $a_{\rm min} \simeq R_{\rm L}/0.38 \gtrsim 8\, R_\odot (R_\star / 3\, R_\odot)$ (Eggleton 1983).

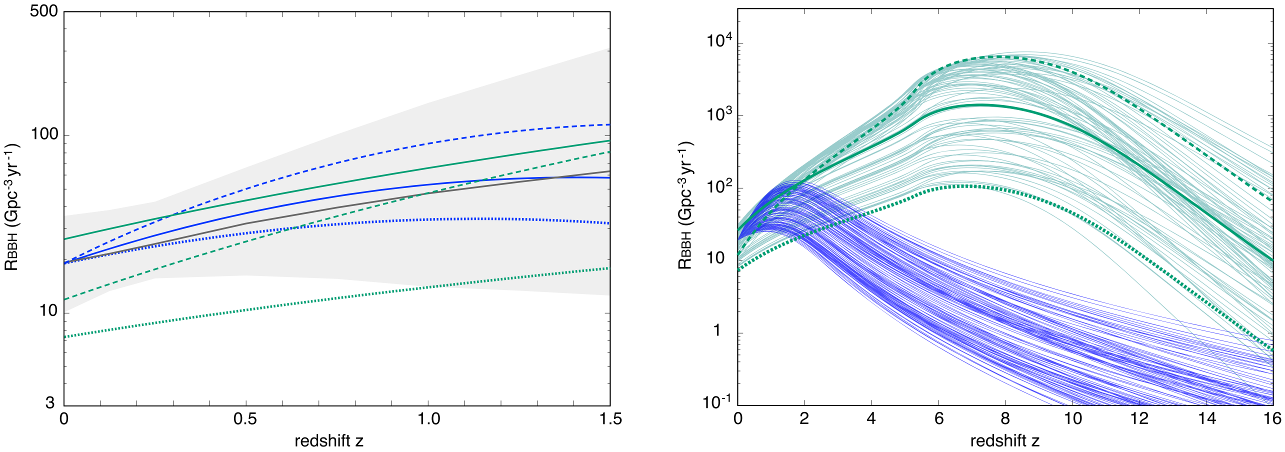

Figure 4. Redshift-dependent BBH merger rates for the low-z (blue) and high-z (green) BBH populations. While the merger rate for the low-z BBHs is normalized to be the observed merger rate at $z = 0$, the normalization for the high-z BBHs is given by the merging-BBH formation efficiency of $f_{\rm BBH} = 0.018$ (see Section 3.2). Left panel: We adopt the DTD index of $n = 0.7$ (dotted), 1.0 (solid), and 1.5 (dashed) and minimal merger time of $t_{\rm min} = 50$ Myr. The redshift dependence of all the models at lower redshifts ($z \lesssim 1.5$) is overall consistent with that inferred from the LIGO-Virgo observing O3a run (shaded region; Abbott et al. 2021a). Right panel: 100 different rates are generated by assuming that n and $t_{\rm min}$ are distributed uniformly over the range of $0.7 \leqslant n \leqslant 1.5$ and $10 \leqslant t_{\rm min}/{\rm Myr} \leqslant 100$. The three cases shown in the left panel are highlighted with the green thick curves. The merger rates for the high-z BBHs rise to $R_{\rm BBH,peak} \sim 10^{3-4}$ Gpc^{-3} yr^{-1} at $z \sim 6$–10, which are $\sim$10–100 times higher than those for the low-z BBHs, even though the expected BBH merger rates at $z \simeq 0$ for the both populations are comparable.

stars (see Sections 2.3 and 4.2). On the other hand, the merging-BBH formation efficiency for the low-z population is determined so that the local merger rate of the low-z BBHs equals the observed GW event rates of $R_{\rm BBH,0} = 19.1\ {\rm Gpc^{-3}\ yr^{-1}}$. This method allows us to avoid numerous uncertainties in modeling of the metallicity effect on the stellar evolution and binary interaction. The cumulative low-z stellar mass density reaches $\rho_\star \simeq (0.5 - 1.6) \times 10^8\ M_\odot\ {\rm Mpc^{-3}}$ by $z \gtrsim 2$–3 before the cosmic noon, when metal enrichment of the universe has not proceeded yet but low-metallicity environments with $Z < Z_{\rm crit}$ still exist. Therefore, the merging-BBH formation efficiency for the high-z population needs to be at least $\gtrsim$20 times higher than that for the low-z population so that both the populations lead to a comparable GW event rate in the local universe (assuming that the two populations follow the same mass spectrum and DTD). We also note that if metal-poor environments are not required for BBH formation, the ratio of the two efficiencies is boosted up to $\simeq$300. This higher contrast is required because the total stellar mass for the low-z population (without the metallicity condition) is $\sim$60 times higher than that of the high-z population and a larger number of the low-z BBHs can merge at $z \simeq 0$ with shorter coalescence timescales.

It is worth giving an analytical formula of the merger rate at $z \simeq 0$ for the high-z BBH population. We approximate their SFRD as $\dot{\rho}_\star \simeq \rho_\star \delta(t - t_0)$ because their formation has terminated in a short duration and the detailed star formation history does not matter as long as those stars form at sufficiently higher redshifts; we adopt $t_0 \simeq 680$ Myr ($\ll t_{\rm H}$) corresponding to the cosmic time at $z \simeq z_{\rm reion}^{50\%}$. Therefore, the merger rate is simply expressed by

$$R_{\rm BBH} \simeq \frac{f_{\rm BBH}\,\rho_\star \Psi_0}{\langle M_{\rm tot,b}\rangle t_{\rm min}} \left(\frac{t}{t_{\rm min}}\right)^{-n}$$
$$\simeq \begin{cases} \dfrac{f_{\rm BBH}\,\rho_\star}{\langle M_{\rm tot,b}\rangle \ln(t_{\rm max}/t_{\rm min})} \cdot \dfrac{1}{t} & \text{for } n = 1, \\[2ex] \dfrac{f_{\rm BBH}\,\rho_\star}{\langle M_{\rm tot,b}\rangle} \dfrac{(n-1)t_{\rm max}^n}{t_{\rm min} t_{\rm max}^n - t_{\rm max} t_{\rm min}^n} \left(\dfrac{t}{t_{\rm min}}\right)^{-n} & \text{for } n \neq 1, \end{cases} \qquad (17)$$

where $t \simeq t_{\rm H}(\gg t_0)$ is considered. Using Equation (17), the local rate is estimated as $R_{\rm BBH} \simeq 29\ {\rm Gpc^{-3}\ yr^{-1}}$ for $n = 1$ ($f_{\rm BBH} = 0.018$, $\rho_\star = 10^7\ M_\odot\ {\rm Mpc^{-3}}$, $\langle M_{\rm tot,b}\rangle = 35\ M_\odot$, $t_{\rm min} = 50$ Myr, and $t_{\rm max} = 10^3\ t_{\rm H}$).

3.3. Redshift-dependent Merger Rates of the Two BBH Populations

In Figure 4, we show the redshift-dependent BBH merger rates for the low-z (blue curves) and high-z (green curves) BBH populations. In the left panel, each curve is generated by setting $t_{\rm min} = 50$ Myr and $n = 0.7$ (dotted), 1.0 (solid), and 1.5 (dashed). The redshift dependence of all the models at lower redshifts ($z \lesssim 1.5$) is overall consistent with that inferred from the LIGO-Virgo O3a run (Abbott et al. 2021a; 90% credible intervals shown by the gray shaded band). The merger rates for the high-z BBHs are well described by Equation (17) and could explain most GW events observed at $z \simeq 0$ in terms of the rate, only if the merging-BBH formation efficiency is as high as $f_{\rm BBH} \simeq 2\%$ (note that the merger rate scales with the value of $f_{\rm BBH}$).

In the right panel, we show the BBH merger rates for the two populations extending the redshift range up to $z = 16$. For each model, we generate 100 different rates by assuming that the power-law index n and the minimum merger time are distributed uniformly over the range of $0.7 \leqslant n \leqslant 1.5$ and $10 \leqslant t_{\rm min}/{\rm Myr} \leqslant 100$ (the three cases with $t_{\rm min} = 50$ Myr shown in the left panel are highlighted with green thick curves). For the low-z population, the merger rates have peaks of $R_{\rm BBH,peak} \sim 30$–$100\ {\rm Gpc^{-3}\ yr^{-1}}$ at the epoch when the cosmic star formation rate is the highest, and decreases toward higher redshifts. In contrast, for the high-z population, a vast majority of the BBHs merge in the early universe at $z \simeq 6$–10 and a small fraction of them (binaries with wider orbital separations at birth) merge within the LIGO/Virgo detection horizon. For the high-z BBH population, the shape of the merger rate depends on the DTD index more sensitively. For the canonical case ($n = 1$; solid), the merger rate increases to $R_{\rm BBH,peak} \sim 10^3\ {\rm Gpc^{-3}\ yr^{-1}}$ at $z \sim 6$–10, which is >10 times higher than for the low-z BBHs, even though the expected local rate is similar to that for the low-z BBH population. With the larger DTD indices ($n = 1.5$; dashed), most BBHs merge at

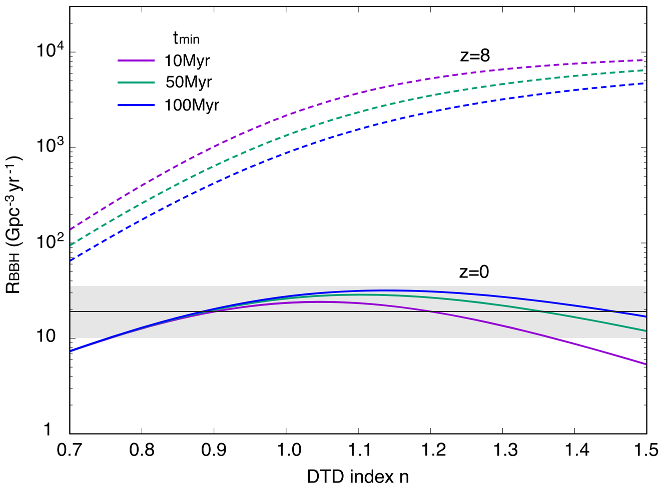

Figure 5. Summary of the dependence of the merger rates for the high-z BBHs at $z = 0$ (solid) and $z = 8$ (dashed) on the DTD index n. Each curve corresponds to the case with different minimum merger time: $t_{\rm min} = 10$ (purple), 50 (green), and 100 Myr (blue).

higher redshifts at a peak rate of $\sim 6 \times 10^3$ Gpc^{-3} yr^{-1}, but the rate quickly decays toward $z \simeq 0$ because the total mass of BBHs is fixed. With the smaller DTD indices ($n = 0.7$; dotted), most BBHs do not merger within a Hubble time and thus both the peak and local rate are significantly lowered.

In Figure 5, we summarize the dependence of the high-z BBH merger rates on the DTD index n. Here, we focus on the merger rate at $z = 0$ (solid curves) and $z = 8$ (dashed), when the rate is maximized. Each curve corresponds to the case with different minimum merger time: $t_{\rm min} = 10$ (purple), 50 (green), and 10 Myr (blue). As also seen in Figure 4, the local merger rate is maximized at $n \simeq 1$ because a good fraction of BBHs formed at $z > z_{\rm reion}$ merge within a Hubble timescale. With a shorter $t_{\rm min}$, the local rate decreases but the peak rate at $z \sim 8$ increase, reflecting the conservation of the total BBH mass budget. The local rate depends on $t_{\rm min}$ only when the DTD index is larger than unity, i.e., the normalization of the DTD determined by the choice of $t_{\rm min}$. Overall, the merger rates for a wide range of the DTD parameters explain the local GW event rate inferred from the LIGO-Virgo O3a observing run (gray region). The peak merger rate increases with the DTD index but approaches $\mathcal{R}_{\rm BBH} \sim 10^4$ Gpc^{-3} yr^{-1} at $n \gtrsim 1.3$. We note that the apparent maximum rate corresponds to the case where all the BBHs immediately merger at birth: $\mathcal{R}_{\rm BBH} \sim f_{\rm BBH}\,\dot{\rho}_\star / \langle M_{\rm tot,b}\rangle \simeq 1.6 \times 10^4$ Gpc^{-3} yr^{-1}.

Finally, we briefly mention the merger rate of BBHs originating from Population III stars. As discussed in Section 2.3 (see Figure 3), the upper limit of the mass density for Population III stars is limited below $\rho_{\star,\rm III} \lesssim 2 \times 10^5\,M_\odot$ Mpc^{-3}, which is $\sim$2% of that for the normal Population II stars. Therefore, even if Population III BBHs follow the DTD with $n \simeq 1.0$, the merger rate of Population III BBHs at $z \simeq 0$ would be as small as $\mathcal{R}_{\rm BBH,III} \simeq 0.5\,(f_{\rm BBH}/0.018)(\langle M_{\rm tot,b}\rangle/35\,M_\odot)^{-1}$ Gpc^{-3} yr^{-1}. This indicates that they could contribute to the local GW events, *only if* $\gtrsim$*40% of all the mass in Population III stars would be converted into BBHs merging within a Hubble time*. Recently, Kinugawa et al. (2021) claimed that BBHs originating from Population III remnants could explain the local GW event rate at $M_1 \gtrsim 30\,M_\odot$, which is responsible for $\sim$10 Gpc^{-3} yr^{-1} and requires $f_{\rm BBH} \simeq 0.5$ for $\langle M_{\rm tot,b}\rangle = 50\,M_\odot$ (note that they adopt $q = 0.7$). Such a high merging-BBH formation efficiency could be provided for a top-heavy IMF (e.g., a flat IMF with a mass range of 10–100 $M_\odot$; $f_\bullet \simeq 0.96$), a high binary fraction $f_{\rm bin} \simeq 1$, and $f_{\rm mrg} \gtrsim 0.5$ (e.g., the distribution of primordial binary separations prefer close binaries; see also Inayoshi et al. 2017). Dynamical capture of BHs in dense metal-free clusters would also form tightly bound BBHs (Liu & Bromm 2020b).

4. Gravitational Wave Background

We next calculate the spectrum of a GWB produced from BBHs that merge at the rates shown in Figure 4:

$$\rho_c c^2 \Omega_{\rm gw}(f) = \int_{z_{\rm min}}^{\infty}\int_{M_{\rm min}}^{M_{\rm max}} \frac{d\mathcal{R}_{\rm BBH}}{dM_1}\left(f_r\frac{dE_{\rm gw}}{df_r}\right)\frac{dt}{dz}\frac{dM_1 dz}{1+z}, \tag{18}$$

(Phinney 2001), where f and f_r are the GW frequencies observed at $z = 0$ and in the source's rest frame, i.e., $f_r = f(1 + z)$, and ρ_c is the critical density of the universe. We set the minimum redshift to $z_{\rm min} = 0.28$, the detection horizon of LIGO-Virgo.[12] The GW spectrum from a coalescing BBH is given by

$$\frac{dE_{\rm gw}}{df_r} = \frac{(\pi G)^{2/3} M_c^{5/3}}{3 f_r^{1/3}}\mathscr{F}_{\rm PN}, \tag{19}$$

where $E_{\rm gw}$ is the energy emitted in GWs, $M_c \equiv (M_1 M_2)^{3/5}/(M_1 + M_2)^{1/5}$ is the chirp mass, M_2 is the secondary mass, and $\mathscr{F}_{\rm PN}$ is the post-Newtonian correction factor (Ajith et al. 2011). We here consider merger events of equal-mass binaries to be consistent with previous works (Abbott et al. 2016a, 2019), which differ from the conditional mass-ratio q distribution of q^{β_q} ($\beta_q = 1.4^{+2.5}_{-1.5}$ for the broken power-law mass spectrum) inferred from the observed merger events (Abbott et al. 2021a). We note that assuming $q = 0.7$, the GWB amplitude shown below is reduced at most by a factor of $\simeq$1.3 ($\simeq$80%) at $f < 100$ Hz. This level of small reduction would be absorbed in the uncertainties of β_q and other model parameters characterizing the primary mass function. We also assume that the orbits of BBHs that contribute to a GWB are circularized by the time they move into the LIGO-Virgo band and thus the GWB spectrum in the inspiral phase scales with frequency as $\Omega_{\rm gw}(f) \propto f^{2/3}$. While binary-single interactions can produce high-eccentricity events, they are likely to constitute a significant fraction of all events only in the AGN disk models (e.g., Samsing et al. 2020; Tagawa et al. 2020).

4.1. The Mass Function of BBH Mergers Consistent with Locally Detected GW Sources

First, we consider BBH mergers whose mass function follows the broken power law provided by the most updated samples of locally detected GW sources (see Equation (11)). We assume that the mass function shape does not evolve with redshift, while the mass-integrated merger rate evolves as shown in Section 3.2.

---

[12] Given the GW sensitivity curve, the size of the observational horizon for a BBH merger depends on the masses of the two BHs. For simplicity, we adopt one single value of the redshift within which BBHs are individually detected. However, the choice weakly affects the estimation of a GWB only for the low-z BBH population if $z_{\rm min} > 0.3$ is set. In this sense, the calculated GWB amplitude for the low-z BBH population corresponds to an upper limit.

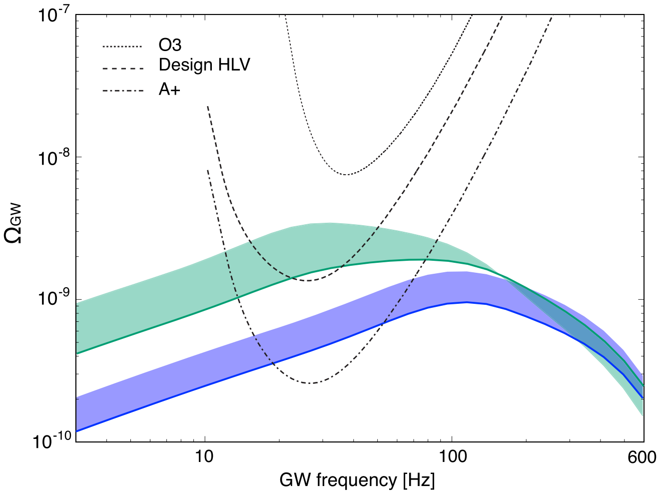

Figure 6. The stochastic GWB spectra produced by the low-z (blue) and high-z (green) BBH populations that follow the merger rates shown in Figure 4. For each case, the shaded region shows the expected GWB amplitude for different DTD parameters, namely, $1.0 \leqslant n \leqslant 1.5$ and $t_{\rm min} = 50$ Myr. The three sensitivity curves of the O3 run (dotted), the HLV design (dashed), and the envisioned A^+ (dotted–dashed) are shown.

In Figure 6, we present the stochastic GWB spectra for the low-z and high-z BBH populations, along with the three sensitivity curves of the O3 run (dotted), the HLV design (dashed), and A^+ (dotted–dashed).[13] The BBH merger rate for each population is shown in Figure 4. The shaded regions show the expected GWB amplitude for different DTD indices at $1.0 \leqslant n \leqslant 1.5$ (the solid curves for $n = 1.0$). The minimum merger time is set to $t_{\rm min} = 50$ Myr for the two populations since the GWB amplitude hardly depends on the choice as long as $t_{\rm min}$ is much less than $\sim$10 Gyr.

For the low-z BBHs, regardless of the model uncertainties, the spectral shape of the GWB is characterized by a well-known (lowest Newtonian order) power law of $\Omega_{\rm gw}(f) \propto f^{2/3}$ at $f < 100$ Hz and peaks at higher frequencies (for comparison, see Abbott et al. 2016a). The GWB amplitude is as low as $\Omega_{\rm gw} \simeq 4.14^{+1.87}_{-1.45} \times 10^{-10}$ at $f = 25$ Hz, where the LIGO-Virgo detectors are the most sensitive. As already pointed out in Abbott et al. (2021b), the weak GWB signal is not detectable at the LIGO-Virgo design sensitivity, but requires the envisioned A^+ sensitivity to be detected.

For the high-z BBHs, the GWB amplitude is as high as $\Omega_{\rm gw} \simeq 1.48^{+1.80}_{-1.27} \times 10^{-9}$ at $f = 25$ Hz. The GWB spectrum is significantly flatter at $f \gtrsim 20$–30 Hz from the value of $2/3$ and peaks inside the frequency window of the LIGO-Virgo observations. This characteristic spectral shape predicted by Inayoshi et al. (2016b) still holds in this modeling where the most updated properties of merging BBHs provided in the GWTC-2 catalog is used. Note that the detailed properties of the spectral flattening depends on model parameters as seen in previous studies (Inayoshi et al. 2016b; Périgois et al. 2021). Even if the constraint from cosmic reionization is taken into account, the GWB signal is still detectable at the HLV design sensitivity. Moreover, if the DTD index is larger than unity, the unique feature of the GWB spectrum can be detected with the HLV design sensitivity. In addition, the detection of this level of GWB would indicate a major contribution by the high-redshift BBH population to the local GW events.

The existence of such individually undetectable BBH mergers beyond the detection horizon also serve as a source of GW events that can be gravitationally lensed by the foreground structures (e.g., Dai et al. 2017; Oguri 2018; Contigiani 2020; Mukherjee et al. 2021). However, Buscicchio et al. (2020) recently showed that even assuming a merger rate at $z > 1$ high enough to produce a GWB detectable at the HLV design sensitivity, the lensing probability for individually detected BBH mergers is as small as $\lesssim 10^{-3}$ over 2 yr of operation. Therefore, if the high-z BBHs contribute to the production of a GWB at the predicted level, we will be able to detect the GWB before a lensed GW source is detected.

4.2. The Upper Bound of GWBs Produced from High-z BBHs with More Top-heavy Mass Function

As an alternative model, we consider a high-z BBH population that follows a mass function more top heavy than the broken power-law one adopted in the fiducial model. This is motivated by the absence of high-mass BBH detections at low redshifts indicating that the astrophysical BBH mass distribution evolves and/or the largest BBHs only merge at high redshifts (Fishbach et al. 2021). Moreover, a top-heavy mass function is expected from cosmological simulations of high-z star formation (e.g., Hirano et al. 2014), BBH formation channels (Kinugawa et al. 2014; Inayoshi et al. 2017), and possible subsequent growth processes via gas accretion in protogalaxies and/or disks in AGN (Safarzadeh & Haiman 2020; Tagawa et al. 2020; see also Inayoshi et al. 2016a).

In Figure 7, we present the GWB amplitudes for three high-z BBH populations whose merger mass function is given by the broken power-law function with $M_{\rm min} = 3.96\,M_\odot$ (green; fiducial case), $M_{\rm min} = 10\,M_\odot$ (purple), and $M_{\rm min} = 30\,M_\odot$ (blue). For the top-heavy models, the average mass of the primary BH is $\langle M_1 \rangle = 26$ and $47\,M_\odot$, respectively, which are used for estimating the merger rate (see Equation (14)). The shaded region presents the expected GWB signal in each model, associated with the possible range of the DTD index; the solid curve is for $n = 1.0$ and the highest value at lower frequencies is for $n = 1.5$. Note that for the top-heavy models, the contribution from BBHs with $3.96\,M_\odot < M_1 < M_{\rm min}$ to the GWB is not included in Figure 7.

With the higher minimum mass, the peak frequency of the GWB moves to a lower value and thus the flattening of the spectrum becomes more prominent compared to the fiducial case (green). The peculiar spectral indices are substantially lower than the canonical value of $\sim 2/3$ expected from lower-z and low-mass BBH mergers. Even with the constraint from cosmic reionization, the expected GWBs for the two top-heavy models are as strong as $\Omega_{\rm gw} \simeq 3.8 \times 10^{-9}$ at $f = 25$ Hz for $M_{\rm min} = 10\,M_\odot$ and $\Omega_{\rm gw} \simeq 4.5 \times 10^{-9}$ at $f = 20$ Hz for $M_{\rm min} = 30\,M_\odot$, which are well above the detection thresholds with the HLV design sensitivity. A detection of such a unique spectrum with the design sensitivity would allow us to extract information on a top-heavy-like mass function of the high-z BBH merger population.

It is worth providing an analytical expression of the GWB upper bound constrained by the history of cosmic reionization. Here, we consider the total GWB energy density calculated

---

[13] HLV stands for LIGO-Hanford, LIGO-Livingston, and Virgo; https://dcc.ligo.org/LIGO-G2001287/public.

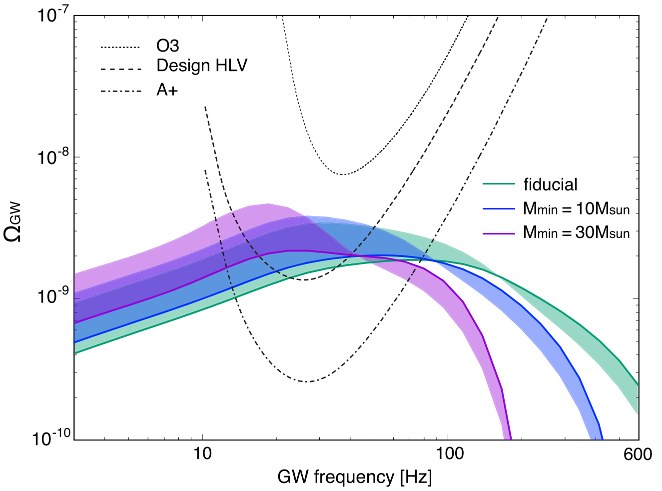

Figure 7. Same as in Figure 6 but with different top-heavy merger mass functions with $M_{\rm min} = 3.96$ (green, fiducial case), 10 $M_\odot$ (blue), and 30 $M_\odot$ (purple). The shaded region presents the expected GWB signal in each model with a DTD index between $1.0 \leqslant n \leqslant 1.5$ (the solid curve for $n = 1.0$). When the high-z BBHs follow more top-heavy mass functions than in the local universe, the spectral shape is skewed toward lower frequencies and the characteristic flattening is detectable at the HLV design sensitivity.

with

$$\mathcal{E}_{\rm GW} \equiv \int_0^\infty \rho_c c^2 \Omega_{\rm gw}(f)\frac{df}{f},$$

$$= \eta_{\rm gw} c^2 \int_{z_{\rm min}}^\infty \left[\int_{M_{\rm min}}^{M_{\rm max}} q M_1 \frac{d\mathcal{R}_{\rm BBH}}{dM_1} dM_1\right]\frac{dt}{dz}\frac{dz}{1+z}, \tag{20}$$

where the GW radiative efficiency is approximated as a constant value of $\eta_{\rm gw} \simeq 0.1$, which is valid for $q > 1/3$. Using Equations (14) and (17), the above equation is approximated as

$$\frac{\mathcal{E}_{\rm GW}}{\rho_c c^2} \simeq \frac{\eta_{\rm gw} f_{\rm BBH} \rho_\star}{\rho_c} \cdot \frac{q}{1+q}\mathcal{I}_n, \tag{21}$$

where

$$\mathcal{I}_n \equiv \int_{t_0+t_{\rm min}}^{t_{\rm H}} \frac{\Psi(t-t_0)}{1+z}dt, \tag{22}$$

which is numerically calculated as $\mathcal{I}_{1.5} \simeq 0.164$, $\mathcal{I}_{1.0} \simeq 0.110$, and $\mathcal{I}_{0.7} \simeq 0.031$. Here, the SFRD is approximated $\dot{\rho}_\star \simeq \rho_\star \delta(t - t_0)$, t_0 ($\simeq$680 Myr) corresponds to the cosmic time at $z \simeq z_{\rm reion}^{50\%}$, and the typical mass ratio does not evolve significantly. In conclusion, we obtain the upper bound on the total GWB energy density

$$\frac{\mathcal{E}_{\rm GW}}{\rho_c c^2} \simeq 8.0 \times 10^{-9}\left(\frac{2q}{1+q}\right)\left(\frac{\eta_{\rm gw}}{0.1}\right)\left(\frac{\mathcal{I}_n}{0.1}\right)$$

$$\times \left(\frac{f_{\rm BBH}}{0.02}\right)\left(\frac{\rho_\star}{10^7\, M_\odot\ {\rm Mpc}^{-3}}\right). \tag{23}$$

We note that the total GWB energy density is independent of the merger mass function. Depending on the GWB spectral shape, which *does* depend on the mass function of BBH mergers, a fraction of the total GWB energy is distributed in the frequency band where the ground-based GW detectors are sensitive.

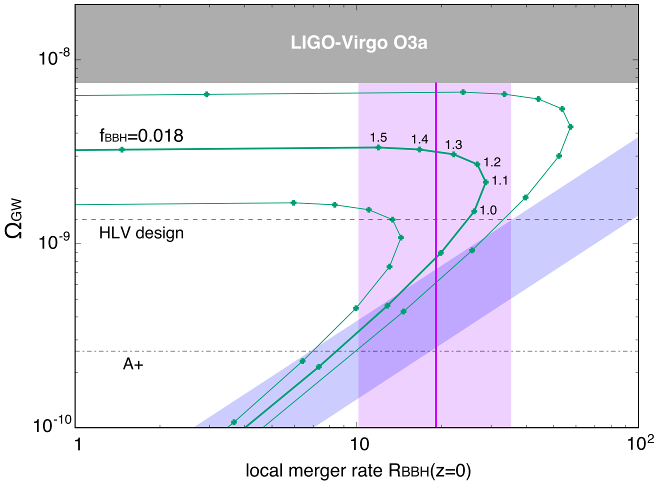

Figure 8. The relation of the GWB amplitude at $f = 25$ Hz and the local BBH merger rate for the low-z (blue region; $0.7 \leqslant n \leqslant 1.5$) and high-$z$ BBH (green curves; $f_{\rm BBH}/0.018 = 0.5$, 1.0, and 2.0) population. The GWB amplitude for the high-z BBHs increases with the DTD index (denoted by the numbers in the figure), while the local merger rate is maximized for $n \sim 1.0$–1.2. In the fiducial case ($f_{\rm BBH} = 0.018$; thick curve), the GWB is detectable at the design sensitivity when the DTD index is in $1.0 \lesssim n \lesssim 1.5$, where the expected local merger rate agrees with the observed GW event rates (magenta region; $R_{\rm BBH,0} = 19.1^{+16.2}_{-9.0}$ Gpc^{-3} yr^{-1}). The current upper limit obtained from the LIGO-Virgo O3a observing run (Abbott et al. 2021b) gives a constraint of $f_{\rm BBH} \lesssim 0.04$.

4.3. The Relation between Ω_{gw}, $R_{BBH,0}$, and Reionization Parameters

In Figure 8, we summarize the relation of the GWB amplitude at $f = 25$ Hz and the local BBH merger rate for each population with different model parameters. For the low-z BBH population (blue region), the expected GWB amplitude is assumed to be proportional to the local merger rate. For a given local merger rate, the GWB amplitude increases with the DTD index ($0.7 \leqslant n \leqslant 1.5$), but it is not detectable at the HLV design sensitivity. For the high-z BBH population (green curves), the GWB amplitude increases with the DTD index (denoted by the numbers in the figure), while the local merger rate is maximized for $n \sim 1.0$–1.2, where the distribution of BBH mergers is spread logarithmically in time and thus a good fraction of BBH mergers occur at $z \simeq 0$. As shown in Figure 5, the local merger rate decreases for smaller and larger DTD indices because most mergers will be pushed into the future ($n < 1$) or occurred well before $z \sim 0$ ($n > 1$). In the fiducial case ($f_{\rm BBH} = 0.018$; thick curve), the GWB is detectable at the design sensitivity when the DTD index is in $1.0 \lesssim n \lesssim 1.5$, where the expected local merger rate agrees with the observed GW event rates (magenta region; $R_{\rm BBH,0} = 19.1^{+16.2}_{-9.0}$ Gpc^{-3} yr^{-1}). Therefore, once this level of GWB will be detected in the O5 observing run, this would indicate a major contribution of the high-z BBH population to the local GW events. If the merging-BBH formation efficiency for the high-z population is substantially less than $\sim$1%, the high-z BBH population neither produces a GWB detectable at the design sensitivity nor explains the local merger rate. In this case, the low-z BBH population dominates the local event rate and a GWB owing to the low-z BBH population would be detected at the envisioned A$^+$ sensitivity. Additionally, the current upper limit of the stochastic GWB obtained from the LIGO-Virgo O3a observing run (Abbott et al. 2021b) gives a constraint of $f_{\rm BBH} \lesssim 0.04$.

The constraint on $f_{\rm BBH}$ from the GWB detection would also be expressed as the relation between the number of BBHs ($q = 1$ is assumed) and ionizing photons produced from the same stellar mass budget. From Figure 8, we obtain

$$\frac{\#\rm BBH}{\#\rm photon} = \frac{f_{\rm bin}}{1+f_{\rm bin}} \frac{m_{\rm p} f_{\bullet}}{\eta_{\rm ion} \langle M_{\bullet} \rangle}, \\ \simeq 3.2 \times 10^{-64} \left(\frac{\langle M_{\bullet} \rangle}{20\, M_{\odot}}\right)^{-1} \left(\frac{f_{\rm esc}}{0.1}\right) \left(\frac{\Omega_{\rm gw,25Hz}}{1.5 \times 10^{-9}}\right), \qquad (24)$$

where $\langle M_{\bullet} \rangle$ is the average BH mass for a given IMF, other parameters are fixed to their fiducial values, and the DTD index is set to $n = 1.0$. Note that we here neglect the extra numerical factor of $(f_{\rm esc}\eta_{\rm ion}/400)^{0.2}$. Therefore, a detection of the GWB at the HLV design sensitivity ($\Omega_{\rm gw} \gtrsim 1.4 \times 10^{-9}$ at $f = 25$ Hz) indicates the existence of a high-z stellar population that forms a few BBHs per $\sim 10^{64}$ ionizing photons.[14] This would give us an insight on the properties of BBH's stellar progenitors (e.g., IMF and metallicity).

4.4. Primordial Binary BHs

Finally, we briefly discuss a GWB produced by BBHs whose formation rate does not necessary follow the cosmic star formation history (e.g., primordial BBH population; see a recent review by Carr et al. 2020). The time dependence of the merger rate is calculated as $R_{\rm BBH} \propto t^{-34/37}$ at $z \ll 1000$ (Nakamura et al. 1997; Sasaki et al. 2016), and the expected GWB amplitude ($f = 25$ Hz) owing to primordial BBHs is as weak as $\Omega_{\rm gw,PBH} \lesssim 10^{-9}$, which is below the HLV design sensitivity, even assuming that all the GW events locally observed originate from the primordial BBH population. This upper bound corresponds to the case where PBHs constitute a fraction of DM, namely, $\Omega_{\rm PBH}/\Omega_{\rm m} \simeq 2 \times 10^{-3}$ (see more arguments in a review paper by Sasaki et al. 2018).

5. Summary and Discussion

In this paper, we consider the GWB produced by BBH mergers originating from the high-z universe at the cosmic dawn. Since overproduction of ionizing photons from stellar progenitors of those BBHs is constrained by the Planck measured optical depth of the universe to electron scattering, the total stellar mass formed during the epoch of reionization has an upper bound. Using a semi-analytical model of the reionization history, we quantify the critical stellar mass density for a metal-enriched Population II stellar population that lead reionization dominantly as $\rho_{\star} \simeq 10^7\, M_{\odot}\,{\rm Mpc}^{-3}$ (see Equation (7)). This value is lowered if other rarer but more intense radiation sources (e.g., metal-free Population III stars) could contribute to reionization.

Under this constraint from the reionization history, the merger rate for the high-z BBH population becomes as high as $R_{\rm BBH} \simeq 5 - 30\,{\rm Gpc}^{-3}\,{\rm yr}^{-1}$ at $z \simeq 0$ for a wide range of the parameters of the DTD for BBH coalescences, where the merging-BBH formation efficiency is assumed to be as high as $f_{\rm BBH}\,(\equiv \dot{\rho}_{\rm BBH}/\dot{\rho}_{\star}) \simeq 0.02$. Since a vast majority of the BBHs merge in the early universe, the merger rate increases to $R_{\rm BBH} \simeq 10^{3-4}\,{\rm Gpc}^{-3}\,{\rm yr}^{-1}$ at $z \simeq 6$–10 for the DTD index of $1.0 \lesssim n \lesssim 1.5$. As a result of their frequent mergers, the amplitude of the GWB produced by the high-z BBH population can be $\Omega_{\rm gw} \simeq 1.48^{+1.80}_{-1.27} \times 10^{-9}$ at $f = 25$ Hz, where the Advanced LIGO-Virgo detectors are the most sensitive. The GWB spectrum is significantly flattened at $f \gtrsim 20$–30 Hz from the value of 2/3 and peaks inside the frequency window of the LIGO-Virgo observations. Note that the flattened spectrum was predicted by previous studies (Inayoshi et al. 2016b; Périgois et al. 2021) but the conclusion still holds even with the BBH properties updated from the LIGO-Virgo O3a observing run and with the new Planck estimated value of $\tau_{\rm e}$. This strong and characteristic GWB signal is detectable at the Advanced LIGO-Virgo design sensitivity. The detection of this level of GWB would also indicate a major contribution of the high-z BBH population to the local GW events.

We also consider a high-z BBH population that follows a mass function more top heavy than in the local universe, motivated by the expected nature of high-z star formation (e.g., Hirano et al. 2014), BBH formation channels (Kinugawa et al. 2014; Inayoshi et al. 2017), and possible subsequent growth processes via gas accretion (Inayoshi et al. 2016a; Safarzadeh & Haiman 2020; Tagawa et al. 2020). With a mass spectrum with a higher minimum mass, the peak frequency of the GWB moves to a lower value and thus the flattening of the spectrum becomes more prominent; namely, the spectral index becomes negative at $f > 20$ Hz. Even with the constraint from cosmic reionization, the GWB strength becomes as strong as $\Omega_{\rm gw} \simeq 4 \times 10^{-9}$ at $f = 20$–25 Hz. A detection of such a unique spectrum with the design sensitivity would allow us to extract information on a top-heavy-like mass function of the high-z BBH merger population.

Finally, we discuss the relation of the GWB amplitude and the local BBH merger rate in Figure 8. In our fiducial case, where the merging-BBH formation efficiency is set to $f_{\rm BBH} \simeq 0.02$, the GWB produced by the high-z BBHs is detectable at the design sensitivity and then those BBHs merge within the Advanced LIGO-Virgo detection horizon at a rate comparable to the observed rate. If the high-z BBHs form at a low efficiency of $f_{\rm BBH} \lesssim 0.01$, the high-$z$ BBH population neither produces a GWB detectable at the design sensitivity nor explains the local merger rate. In this case, the low-z BBH population dominates the local event rate and a GWB owing to the low-z BBH population would be detected at the envisioned A$^+$ sensitivity. In addition, the current upper limit of the stochastic GWB obtained from the LIGO-Virgo O3a observing run (Abbott et al. 2021b) gives a constraint of $f_{\rm BBH} \lesssim 0.04$.

K.I. acknowledges support from the National Science Foundation of China (11721303, 11991052, 11950410493) and the National Key R&D Program of China (2016YFA0400702). K.K. acknowledges support from the JSPS KAKENHI grant Nos. JP20K04010 and JP20H01904. E.V. acknowledges support from NSF grant AST-2009309. Z.H. acknowledges support from NASA through grant 80NSSC18K1093 and from the National Science Foundation through grants 1715661 and 2006176.

ORCID iDs

Kohei Inayoshi https://orcid.org/0000-0001-9840-4959
Kazumi Kashiyama https://orcid.org/0000-0003-4299-8799
Eli Visbal https://orcid.org/0000-0002-8365-0337
Zoltán Haiman https://orcid.org/0000-0003-3633-5403

References

Abbott, B. P., Abbott, R., Abbott, T. D., et al. 2016a, PhRvL, 116, 131102
Abbott, B. P., Abbott, R., Abbott, T. D., et al. 2016b, ApJL, 818, L22
Abbott, B. P., Abbott, R., Abbott, T. D., et al. 2016c, PhRvL, 116, 061102

---

[14] This efficiency of #BBH/#photon shown here ($q = 1$ is assumed) is ~10 times higher than that given in Figure 2 of Inayoshi et al. (2016b), where the binary mass ratio follows a flat distribution.

Abbott, B. P., Abbott, R., Abbott, T. D., et al. 2019, PhRvX, 9, 031040
Abbott, R., Abbott, T. D., Abraham, S., et al. 2021a, PhRvX, 11, 021053
Abbott, R., Abbott, T. D., Abraham, S., et al. 2021b, PhRvD, 104, 022004
Ade, P. A. R., Aghanim, N., Arnaud, M., et al. 2016, A&A, 594, A13
Ahn, K., & Shapiro, P. R. 2021, ApJ, 914, 44
Ajith, P., Hannam, M., Husa, S., et al. 2011, PhRvL, 106, 241101
Ali-Haïmoud, Y., Kovetz, E. D., & Kamionkowski, M. 2017, PhRvD, 96, 123523
Bartos, I., Kocsis, B., Haiman, Z., & Márka, S. 2017, ApJ, 835, 165
Belczynski, K., Repetto, S., Holz, D. E., et al. 2016, ApJ, 819, 108
Boco, L., Lapi, A., Chruslinska, M., et al. 2021, ApJ, 907, 110
Boco, L., Lapi, A., Goswami, S., et al. 2019, ApJ, 881, 157
Bromm, V., & Yoshida, N. 2011, ARA&A, 49, 373
Buscicchio, R., Moore, C. J., Pratten, G., et al. 2020, PhRvL, 125, 141102
Callister, T., Fishbach, M., Holz, D. E., & Farr, W. M. 2020, ApJL, 896, L32
Carr, B., Kohri, K., Sendouda, Y., & Yokoyama, J. 2020, arXiv:2002.12778
Contigiani, O. 2020, MNRAS, 492, 3359
Costa, G., Bressan, A., Mapelli, M., et al. 2021, MNRAS, 501, 4514
Crowther, P. A., Barnard, R., Carpano, S., et al. 2010, MNRAS, 403, L41
Dai, L., Venumadhav, T., & Sigurdson, K. 2017, PhRvD, 95, 044011
Dayal, P., Volonteri, M., Choudhury, T. R., et al. 2020, MNRAS, 495, 3065
Dijkstra, M., Haiman, Z., Rees, M. J., & Weinberg, D. H. 2004, ApJ, 601, 666
Dominik, M., Belczynski, K., Fryer, C., et al. 2012, ApJ, 759, 52
Dvorkin, I., Vangioni, E., Silk, J., Uzan, J.-P., & Olive, K. A. 2016, MNRAS, 461, 3877
Eggleton, P. P. 1983, ApJ, 268, 368
Farmer, R., Renzo, M., de Mink, S. E., Fishbach, M., & Justham, S. 2020, ApJL, 902, L36
Fishbach, M., Doctor, Z., Callister, T., et al. 2021, ApJ, 912, 98
Fragos, T., Lehmer, B., Tremmel, M., et al. 2013, ApJ, 764, 41
Ghirlanda, G., Salafia, O. S., Pescalli, A., et al. 2016, A&A, 594, A84
Greif, T. H., & Bromm, V. 2006, MNRAS, 373, 128
Gruppioni, C., Béthermin, M., Loiacono, F., et al. 2020, A&A, 643, A8
Haiman, Z., & Bryan, G. L. 2006, ApJ, 650, 7
Haiman, Z., & Loeb, A. 1997, ApJ, 483, 21
Hartwig, T., Volonteri, M., Bromm, V., et al. 2016, MNRAS, 460, L74
Hirano, S., Hosokawa, T., Yoshida, N., et al. 2014, ApJ, 781, 60
Inayoshi, K., Haiman, Z., & Ostriker, J. P. 2016a, MNRAS, 459, 3738
Inayoshi, K., Hirai, R., Kinugawa, T., & Hotokezaka, K. 2017, MNRAS, 468, 5020
Inayoshi, K., Kashiyama, K., Visbal, E., & Haiman, Z. 2016b, MNRAS, 461, 2722
Johnson, J. L. 2010, MNRAS, 404, 1425
Johnson, J. L., Dalla, V. C., & Khochfar, S. 2013, MNRAS, 428, 1857
Kinugawa, T., Inayoshi, K., Hotokezaka, K., Nakauchi, D., & Nakamura, T. 2014, MNRAS, 442, 2963
Kinugawa, T., Miyamoto, A., Kanda, N., & Nakamura, T. 2016, MNRAS, 456, 1093
Kinugawa, T., Nakamura, T., & Nakano, H. 2021, MNRAS, 504, L25
Kowalska-Leszczynska, I., Regimbau, T., Bulik, T., Dominik, M., & Belczynski, K. 2015, A&A, 574, A58
Kulkarni, M., Visbal, E., & Bryan, G. L. 2019, ApJ, 882, 178
Liu, B., & Bromm, V. 2020a, MNRAS, 497, 2839
Liu, B., & Bromm, V. 2020b, MNRAS, 495, 2475
Ma, X., Hopkins, P. F., Kasen, D., et al. 2016, MNRAS, 459, 3614
Madau, P., & Dickinson, M. 2014, ARA&A, 52, 415
Madau, P., Haardt, F., & Rees, M. J. 1999, ApJ, 514, 648
Maoz, D., Mannucci, F., & Nelemans, G. 2014, ARA&A, 52, 107
Mapelli, M. 2016, MNRAS, 459, 3432
McKernan, B., Ford, K. E. S., Bellovary, J., et al. 2018, ApJ, 866, 66
Mirabel, I. F. 2019, in IAU Symp. 346, 365
Mirabel, I. F., Dijkstra, M., Laurent, P., Loeb, A., & Pritchard, J. R. 2011, A&A, 528, A149
Moe, M., & Di Stefano, R. 2017, ApJS, 230, 15
Mukherjee, S., Broadhurst, T., Diego, J. M., Silk, J., & Smoot, G. F. 2021, MNRAS, 501, 2451
Nakamura, T., Sasaki, M., Tanaka, T., & Thorne, K. S. 1997, ApJL, 487, L139
Nakauchi, D., Inayoshi, K., & Omukai, K. 2020, ApJ, 902, 81
Neijssel, C. J., Vigna-Gómez, A., Stevenson, S., et al. 2019, MNRAS, 490, 3740
Oguri, M. 2018, MNRAS, 480, 3842
Okamoto, T., Gao, L., & Theuns, T. 2008, MNRAS, 390, 920
O'Leary, R. M., Meiron, Y., & Kocsis, B. 2016, ApJL, 824, L12
Pawlik, A. H., Schaye, J., & van Scherpenzeel, E. 2009, MNRAS, 394, 1812
Périgois, C., Belczynski, C., Bulik, T., & Regimbau, T. 2021, PhRvD, 103, 043002
Phinney, E. S. 2001, arXiv:0108028
Piran, T. 1992, ApJL, 389, L45
Planck Collaboration, Aghanim, N., Akrami, Y., et al. 2020, A&A, 641, A6
Portegies Zwart, S. F., & McMillan, S. L. W. 2000, ApJL, 528, L17
Robertson, B. E., Ellis, R. S., Furlanetto, S. R., & Dunlop, J. S. 2015, ApJL, 802, L19
Rodriguez, C. L., Morscher, M., Pattabiraman, B., et al. 2015, PhRvL, 115, 051101
Safarzadeh, M., Biscoveanu, S., & Loeb, A. 2020, ApJ, 901, 137
Safarzadeh, M., & Haiman, Z. 2020, ApJL, 903, L21
Samsing, J., Bartos, I., D'Orazio, D. J., et al. 2020, arXiv:2010.09765
Sana, H., de Mink, S. E., de Koter, A., et al. 2012, Sci, 337, 444
Sanders, R. L., Shapley, A. E., Jones, T., et al. 2021, ApJ, 914, 19
Santoliquido, F., Mapelli, M., Giacobbo, N., Bouffanais, Y., & Artale, M. C. 2021, MNRAS, 502, 4877
Sasaki, M., Suyama, T., Tanaka, T., & Yokoyama, S. 2016, PhRvL, 117, 061101
Sasaki, M., Suyama, T., Tanaka, T., & Yokoyama, S. 2018, CQGra, 35, 063001
Schaerer, D. 2002, A&A, 382, 28
Schaerer, D. 2003, A&A, 397, 527
Spera, M., & Mapelli, M. 2017, MNRAS, 470, 4739
Stone, N. C., Metzger, B. D., & Haiman, Z. 2017, MNRAS, 464, 946
Suzuki, T. L., Onodera, M., Kodama, T., et al. 2021, ApJ, 908, 15
Tagawa, H., Haiman, Z., & Kocsis, B. 2020, ApJ, 898, 25
Tanikawa, A., Susa, H., Yoshida, T., Trani, A. A., & Kinugawa, T. 2021, ApJ, 910, 30
van den Heuvel, E. P. J., Portegies Zwart, S. F., & de Mink, S. E. 2017, MNRAS, 471, 4256
Visbal, E., Bryan, G. L., & Haiman, Z. 2020, ApJ, 897, 95
Visbal, E., Haiman, Z., & Bryan, G. L. 2015, MNRAS, 453, 4456
Wanderman, D., & Piran, T. 2010, MNRAS, 406, 1944
Wang, T., Schreiber, C., Elbaz, D., et al. 2019, Natur, 572, 211
Wise, J. H., Demchenko, V. G., Halicek, M. T., et al. 2014, MNRAS, 442, 2560
Wise, J. H., Turk, M. J., Norman, M. L., & Abel, T. 2012, ApJ, 745, 50
Woosley, S. E. 2017, ApJ, 836, 244
Wyithe, J. S. B., & Loeb, A. 2003, ApJ, 586, 693
Yung, L. Y. A., Somerville, R. S., Finkelstein, S. L., et al. 2020a, MNRAS, 496, 4574
Yung, L. Y. A., Somerville, R. S., Popping, G., & Finkelstein, S. L. 2020b, MNRAS, 494, 1002